A Multi-channel Wiener Filter Method of Deformation Measurement for Simultaneous Multi-Angle Spaceborne D-InSAR

Yuanhao Li, *Member, IEEE,* Paco López Dekker, *Senior Member, IEEE,* Pau Prats-Iraola, *Senior Member, IEEE*

Abstract—Simultaneous multi-angle spaceborne synthetic aperture radar (SAR) can provide spatially diverse SAR images of the same scene without time lags. Through Differential SAR interferometry (D-InSAR), the system can extract accurate multi-dimensional deformations from the mixing differential tropospheric delay (DTD), which generally distorts deformation signals in single interferograms. This paper focuses on the multi-dimensional deformation estimation by simultaneous multi-angle spaceborne D-InSAR. A multi-channel Wiener filter (MWF)-based multi-dimensional deformation and DTD joint estimation method is proposed in this paper, which achieves the optimal estimation accuracy and reduces the loss of scene details. It was validated by both the simulations based on the system parameters of the future European Space Agency (ESA) Harmony mission and with real TanDEM-X bidirectional (BiDi) SAR data acquired over two scenes in California, USA. We analyzed the performance of the method in the presence of multiple error sources and investigated the impact of different observation geometries on estimation performance. The results not only demonstrate the potential of simultaneous multi-angle spaceborne D-InSAR in multi-dimensional deformation measurement, but also show that the proposed method can achieve good performance in terms of estimation accuracy and preservation of spatial resolution.

Index Terms—Synthetic aperture radar (SAR), differential interferometric SAR (D-InSAR), deformation measurement, multi-angle SAR system.

I. INTRODUCTION

SPACEBORNE differential interferometric synthetic aperture radar (D-InSAR) can retrieve surface deformation exploiting repeat-pass differential interferometric phases [1], [2]. However, using a single differential interferogram for accurate and comprehensive deformation measurements faces challenges. On one hand, atmospheric phase contributions, which are comparable to and even larger than deformation phases [3], seriously pollute deformation phases [4]. On the other hand, through a single differential interferogram, only the displacement of the ground surface along the line-of-sight

Y. Li is with the School of Information and Electronics, Beijing Institute of Technology, 100081, China, and also with the Department of Geoscience and Remote Sensing, Delft University of Technology, Delft, The Netherlands. e-mail: lyh.900101@163.com)

P. López Dekker is with the Department of Geoscience and Remote Sensing, Delft University of Technology, Delft, The Netherlands.

P. Prats-Iraola is with German Aerospace Center (DLR), D-82234 Wessling, Germany.

(LOS) of the satellite can be obtained [5], [6]. Given these limitations in D-InSAR measurement, it is very hard to monitor millimeter-level multi-dimensional surface deformations from geological disaster events.

Solutions to these issues have been studied for many years. Exploiting its dispersive nature, the ionospheric component in the atmospheric phases can be estimated and compensated through the split-spectrum method [7]. The compensation of tropospheric phases remains challenging. Only the low-wavenumber components can be empirically removed using meteorological data and weather models [8]–[10]. D-InSAR time-series processing is the other option to compensate the random atmospheric phases through their uncorrelated behavior in the temporal domain [11], [12]. Nevertheless, its drawback is the required large amount of data in the processing and the need of a prior functional model for the temporal deformation signal. Consequently, this approach proves inadequate for addressing abrupt deformation signals, such as those resulting from volcanic or seismic events [13]. Regarding the measurements of multi-dimensional deformations, interferometric processing with a spectral diversity, global navigation satellite system-assisted (GNSS-assisted) D-InSAR and surface deformation model-assisted D-InSAR are some possible approaches [14]–[18]. However, they are limited by either retrieval accuracy or spatial resolutions.

A simultaneous multi-angle D-InSAR is a feasible solution to address the aforementioned issues. The system will obtain multiple line-of-sights observations diverse in space, which can help retrieve multi-dimensional deformations separately from atmospheric components [19]–[22]. A similar concept was studied by Jet Propulsion Laboratory (JPL) researchers by using the UAVSAR system [23]. However, in that case, the lack of simultaneity in the multi-angle synthetic aperture radar (SAR) data, leading to a partially temporally decorrelated atmosphere introduced too many differential tropospheric delay (DTD) decorrelation phase errors. The Harmony system is a simultaneous multi-angle SAR system [20], [24], which is the only European Space Agency (ESA) Earth Explorer 10 (EE-10) mission candidate entering into the Phase B1 stage at the time of writing. In the Harmony system, the two Harmony passive radar systems receive the multistatically scattered radar signal transmitted by a Sentinel-1 satellite. Considering also the backscattered signals received by Sentinel-1, this results in three simultaneous LOSs. Due to the simultaneous observations and the low altitude of the troposphere, the DTD from each D-InSAR interferogram in the Harmony (or a sim-

ilar) system are highly correlated. Then, using the D-InSAR interferograms of at least three satellites in the simultaneous multi-angle SAR system, the DTD along with two-dimensional (2-D) deformations (the LOS of the reference satellite and its azimuth direction) can be regarded as unknown parameters to be jointly estimated.

Simultaneous multi-angle D-InSAR offers clear advantages in accurately measuring multi-dimensional deformations. First, DTDs and deformation signals can be decoupled without time-series processing, which allows mapping short-time term deformation signals. In addition, since the DTD is directly obtained from D-InSAR data, the effects of the DTD stratification component have been included in the estimation automatically. The estimated DTD can also serve as a valuable by-product to enhance the accuracy of numerical weather forecasting through weather data assimilation [9]. In fact, some initial study of simultaneous multi-angle D-InSAR for deformation and DTD measurement has already been conducted. Prats-Iraola, et al. derived the theoretical deformation estimation sensitivity and verified that N-S deformation measurement accuracy could be improved due to the differentiation of correlated tropospheric phases in the simultaneous multi-angle interferograms [25], [26]. Similarly, considering deformation signals mostly as nuisance noise under short repeat-pass periods, our previous paper [27] focused on the method and performance of directly estimating DTD by simultaneous multi-angle D-InSAR. However, these studies aim at the estimation of either deformations or DTD, while regarding the other component as noise.

When jointly estimating both multi-dimensional deformation and DTD by simultaneous multi-angle D-InSAR, several issues should be specially considered. First, deformations and DTD have obviously distinguished spatial behaviors (e.g., scales and intensities), the estimation without the consideration of this prior knowledge fail to achieve the best estimation performance in accuracy and resolution-preservation. Moreover, besides the errors from thermal noise and orbital errors, uncorrelated atmospheric phases can impact the estimation [25], [28]. Most of these phase components can be attributed to an effective horizontal shift of the tropospheric phase screen as a result from the different observation geometries [23], [27], where the troposphere is implicitly modelled as an infinitesimally thin layer at some effective height above the surface. Since this height is not known, this shift cannot be directly included in the joint estimation of deformation and DTD. The other component derives from uncompensated small-scale ionospheric turbulences even when classical ionospheric effects compensation methods are applied [7]. At last, the performance of joint estimation naturally relies on the spatial diversity of observations, making it valuable to investigate the relationship between estimation performance and observation geometries.

To address the aforementioned issues, we proposed a multi-channel Wiener filter (MWF)-based method in simultaneous multi-angle D-InSAR to jointly estimate both multi-dimensional deformation and DTD. The spatially prior statistical information of multi-dimensional deformation and DTD is utilized to filter each parameter adaptively, which can achieve the optimal performance in accuracy and resolution-

preservation. Additionally, the method's performance under multiple error sources and different observation geometries is also studied.

This paper is organized as follows. The typical observation geometry of a simultaneous multi-angle D-InSAR system is first described in Section II. The observation signal model is established and the main error sources, including thermal noise, orbital errors, uncorrelated DTD components, and uncompensated small-scale ionospheric turbulences, are discussed in detail. In Section III, the proposed MWF-based joint estimation method of multi-dimensional deformation and DTD is described. In Section IV, the effectiveness of the simultaneous multi-angle D-InSAR in the joint estimation and the proposed method is validated with both the simulations based on the system parameters of the Harmony mission and with the multi-angle TanDEM-X bidirectional(BiDi) SAR imaging data [29]. Even though the TanDEM-X system is not a rigorous simultaneous multi-angle SAR system and its observation spatial diversity is not large, it can also provide an insight into the performance of the proposed method. The results show the robustness of the proposed method in the joint estimation under multiple error sources and different geometries. Finally, we conclude the paper in Section V.

II. OBSERVATION SIGNAL MODEL

To illustrate the observation geometry, Fig. 1 shows an example of a simultaneous multi-angle SAR system with four satellites to estimate both three-dimensional (3-D) deformations and DTD by measurements. All satellites fly in formation. In the group, one satellite is defined as the reference, where its LOS ($\hat{l}_r$), azimuth ($\hat{l}_a$), their cross product ($\hat{l}_p$), and the zenith direction ($\hat{z}$) serve as the reference base in the measurement, where a different coordinate, such as the local East, North, Up (ENU) coordinate, can also be an option.

Generally, the troposphere has the following two characteristics: 1) Compared to the height of the satellites, the altitude of the troposphere is relatively low, which is generally 7-20 km high. 2) the DTD is spatially correlated, with a correlation distance of hundreds of meters to a few kilometers, in the absence of small-scale turbulences brought by convective rain. Therefore, the observed DTD by each satellite's D-InSAR interferogram in the simultaneous multi-angle spaceborne SAR system is correlated [27]. Thus, we can model the observed DTD from different satellites by an identical zenith DTD multiplying mapping coefficients and the decorrelation DTD noise.

Considering the observations of four satellites, the obtained D-InSAR interferograms of four satellites $\varphi = [\varphi_{Ref}, \varphi_{C_1}, \varphi_{C_2}, \varphi_{C_3}]^T$ are expressed as

$$\varphi = \mathbf{Hd} + \varphi_n, \qquad (1)$$

where $\mathbf{d} = [d_{los}, d_a, d_p, d_{atm}]^T$ is the estimated vector, including 3-D deformations, i.e., the LOS deformation, d_{los}, the azimuth deformation, d_a, the deformation projected to $\hat{l}_p$, d_p, and the zenith atmospheric delay, d_{atm}. Under the assumption of equivalent single-layer atmosphere it holds that

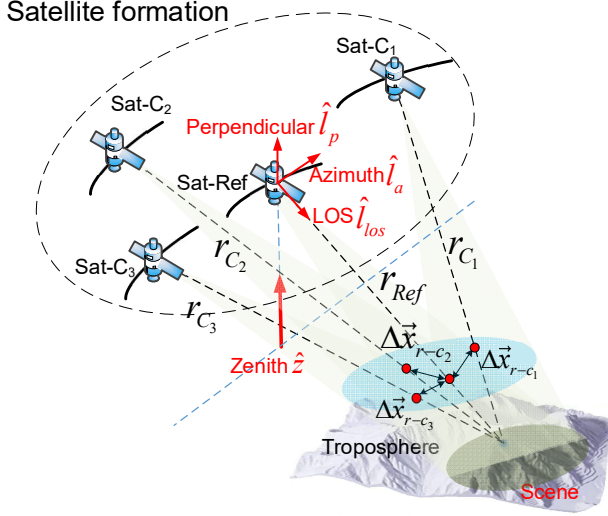Fig. 1. Observation geometry of a simultaneous multi-angle SAR system with four-satellites in formation. $Sat - Ref$, $Sat - C_1$, $Sat - C_2$, and $Sat - C_3$ are the four satellites in formation, their slant ranges are r_{Ref}, r_{C_1}, r_{C_2}, and r_{C_3}, respectively. $Sat - Ref$ is the reference satellite. Its line-of-sight (LOS) $\hat{l}_r$, azimuth $\hat{l}_a$, and their cross product $\hat{l}_p$ serve as the reference basis for measurements, and $\hat{z}$ is the unit vector of its zenith direction. $\Delta\vec{x}_{r-C_1}$, $\Delta\vec{x}_{r-C_2}$, and $\Delta\vec{x}_{r-C_3}$ are the distances between the beam center of the reference satellite and other companions on the effective height of the troposphere.

$$\mathbf{H} = -\frac{4\pi}{\lambda} \begin{bmatrix} \left\langle \hat{r}_{Ref}, \hat{l}_r \right\rangle & \left\langle \hat{r}_{Ref}, \hat{l}_a \right\rangle & \left\langle \hat{r}_{Ref}, \hat{l}_p \right\rangle & \frac{1}{\left\langle \hat{r}_{Ref}, \hat{z} \right\rangle} \\ \left\langle \hat{r}_{C_1}, \hat{l}_r \right\rangle & \left\langle \hat{r}_{C_1}, \hat{l}_a \right\rangle & \left\langle \hat{r}_{C_1}, \hat{l}_p \right\rangle & \frac{1}{\left\langle \hat{r}_{C_1}, \hat{z} \right\rangle} \\ \left\langle \hat{r}_{C_2}, \hat{l}_r \right\rangle & \left\langle \hat{r}_{C_2}, \hat{l}_a \right\rangle & \left\langle \hat{r}_{C_2}, \hat{l}_p \right\rangle & \frac{1}{\left\langle \hat{r}_{C_2}, \hat{z} \right\rangle} \\ \left\langle \hat{r}_{C_3}, \hat{l}_r \right\rangle & \left\langle \hat{r}_{C_3}, \hat{l}_a \right\rangle & \left\langle \hat{r}_{C_3}, \hat{l}_p \right\rangle & \frac{1}{\left\langle \hat{r}_{C_3}, \hat{z} \right\rangle} \end{bmatrix}, \tag{2}$$

$\hat{r}_{Ref}$, $\hat{r}_{C_1}$, $\hat{r}_{C_2}$, and $\hat{r}_{C_3}$ are the range vectors of the reference and three companions satellites, respectively, $\hat{z}$ is the unit vector of the zenith direction, $\langle \cdot \rangle$ represents the inner product operation, λ is the wavelength, $\boldsymbol{\varphi_n}$ is the phase noise vector term.

For a simultaneous multi-angle spaceborne D-InSAR, we should consider more components in φ_n than the general single-satellite D-InSAR, which are expressed by

$$\boldsymbol{\varphi_n} = \boldsymbol{\varphi_{n_c}} + \boldsymbol{\varphi_{n_{ino}}} + \boldsymbol{\varphi_{n_{tr\_de}}} + \boldsymbol{\varphi_{n_b}}, \tag{3}$$

These components relate to the quality of the interferograms, atmospheric conditions, processing algorithms, and system observation geometries, which are specified as follows:

- $\boldsymbol{\varphi_{n_c}}$ is the coherence-related noise term and its standard deviation is expressed as [30]

$$\sigma_{\varphi_{n_c}} = \frac{1}{\sqrt{2N_L}} \frac{\sqrt{1 - \gamma^2}}{\gamma}, \tag{4}$$

where N_L is the number of looks and γ is the correlation coefficient.

- $\boldsymbol{\varphi_{n_{ino}}}$ is the high-frequency phase components from ionosphere after the split-spectrum method is applied and its variance is given by [27]

$$\sigma_{ino}^2 = \iint_{\boldsymbol{F}} \beta S(\mathbf{k}) \, d\mathbf{k}, \tag{5}$$

where $\boldsymbol{F}$ represents the spatial wavenumbers between the wavenumber used in the split-spectrum and that corresponding to the spatial resolutions of interferograms, β is the spectrum coefficient, $\mathbf{k}$ represents the wavenumber vector and $S(\mathbf{k})$ represents the power spectrum density (PSD) of the ionospheric phases.

- $\boldsymbol{\varphi_{n_{tr\_de}}}$ represents spatially uncorrelated DTD phases of different observations in the formation and its variance depends on the spatial distances of the signal paths on the troposphere between the different satellites ($\Delta\vec{x}$) (See Fig. 1) and the intensity of the tropospheric phases. Under an assumption of homogeneous troposphere, the variance of the uncorrelated DTD phases can be expressed by

$$\sigma_{\varphi_{n,tr\_de}}^2 = \iint S_{\text{tr}}(\mathbf{k}) \, d\mathbf{k}, \tag{6}$$

where $S_{\text{tr}}(\mathbf{k})$ is the PSD of the uncorrelated DTD phases under a single layer assumption, which can be written as

$$S_{\text{tr}}(\mathbf{k}) = 2k_r^2 (1 - \cos \mathbf{k}\Delta\vec{x}) S_{\Phi_a(\mathbf{k})}, \tag{7}$$

where k_r is the ratio of the cosine values of the incidence angles between the reference satellite and another satellite in the formation and $S_{\Phi_a(\mathbf{k})}$ is the PSD of the DTD phases, which can generally be modelled by a power-law spectrum under an atmospheric turbulence environment.

- $\boldsymbol{\varphi_{n_b}}$ represents the baseline error phases, which is given by

$$\boldsymbol{\varphi_{n_b}} = -\frac{4\pi}{\lambda} (\boldsymbol{e_h} \sin \boldsymbol{\theta_l} - \boldsymbol{e_v} \cos \boldsymbol{\theta_l}), \tag{8}$$

where $\boldsymbol{\theta_l}$ are the look angle vectors and $\boldsymbol{e_v}$ and $\boldsymbol{e_h}$ are the baseline error vectors in vertical and the horizontal directions, respectively.

III. JOINT ESTIMATION METHODOLOGY

The estimation of $\boldsymbol{d}$ by simultaneous multi-angle D-InSAR observations can be achieved by a fixed-resolution inversion (FRI) through the simple Least-Squares (LS) approach. The estimated vector can be written as [21], [31]

$$\hat{\mathbf{d}} = \left(\mathbf{H}^T \mathbf{W_{LS}} \mathbf{H}\right)^\dagger \mathbf{H}^T \mathbf{W_{LS}} \boldsymbol{\varphi}_{\text{uw}}, \tag{9}$$

where $\mathbf{W_{LS}}$ is the weighting matrix and $\boldsymbol{\varphi}_{\text{uw}}$ is the unwrapped phases of $\boldsymbol{\varphi}$.

In the fixed-resolution inversion, spatial averaging (i.e. multi-looking or spatial moving box averaging) will be applied to suppress uncorrelated phase noise. However, the optimal selection of the filtering window is not trivial because all the estimated parameters before the inversion are coupled. A too large number of looks or a too-small one will either lead to a loss of spatial resolution or to a sub-optimal performance.
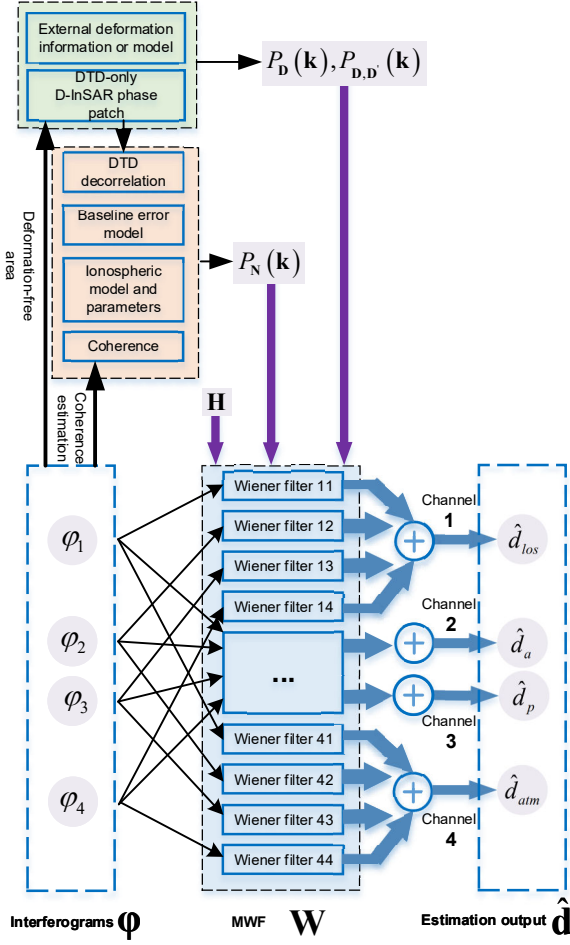
Fig. 2. The sketchmap of the MWF-based for joint estimation of 3D deformation and DTD. $\boldsymbol{H}$ is the observation matrix of the system and $\boldsymbol{N}$ is the noise matrix. $\hat{\boldsymbol{d}}$ is the estimation vector with d_{los}, d_a, d_p are the deformations in the line-of-sight (LOS), azimuth, and their cross product direction, respectively. d_{atm} is the DTD. $\wedge$ represents the estimation values of the parameters. $\boldsymbol{\varphi}$ is the phase vector, where φ_1, φ_2, φ_3, and φ_4 are the D-InSAR phases of the simultaneous multi-angle observations of four satellites. Four sequence sub-channels in the MWF form a channel to filter out one element in the estimation vector.

In general, the deformation components and the DTD have distinct spatial statistics, i.e., spatial correlation lengths and intensity. During the estimation of $\boldsymbol{d}$, each parameter should be filtered optimally according to its statistical behaviour, which will provide a better estimation performance in noise reduction and resolution preservation. For example, if the spatial frequency of the deformation in one direction is much lower than for the other directions, more averaging should be conducted during its inversion. Conversely, a spatially fast-varying deformation component requires less spatial averaging in the corresponding direction. To realize the optimized estimation, a MWF-based for joint estimation of multi-dimensional deformation and DTD in the simultaneous multi-angle D-InSAR is proposed, as sketched in Fig. 2.

To reduce the deduction complicity, we express the estimated vector and the optimization function of the MWF-based method in the wavenumber domain as

$$\begin{cases} \hat{\mathbf{D}}\left(\mathbf{k}\right) = \mathbf{W}\left(\mathbf{k}\right)\boldsymbol{\Phi}\left(\mathbf{k}\right), \\ s.t. \mathbf{W}\left(\mathbf{k}\right) = \arg\min_{W_{i,j}} \xi, \end{cases} \tag{10}$$

where $\hat{\mathbf{D}} = [\hat{D}_{los}, \hat{D}_a, \hat{D}_p, \hat{D}_{atm}]^T$ is the estimated vector of d_{los}, d_a, d_p, and d_{atm} in the wavenumber domain. Here, we use capital letters to indicate the variables in the wavenumber domain while the lowercase letters refer to the spatial domain. Likewise, in the wavenumber domain, $\boldsymbol{\Phi}$ is the unwrapped multi-angle D-InSAR interferogram and $\mathbf{W}$ represets the co-efficients of the MWF. MWF utilizes 16 sub-channels to offer estimations $\hat{\mathbf{D}}$ and the corresponding $\mathbf{W}(\mathbf{k})$ is a 4 by 4 matrix. As shown in Fig. 2, four sequence sub-channels in MWF form a channel ($\mathbf{W}_i(k)(i=1,2,3,4)$ is a row vector in $\mathbf{W}(\mathbf{k})$) to filter out one element in $\hat{\mathbf{D}}$. $\xi = E\left[\left\|\mathbf{D}(\mathbf{k}) - \hat{\mathbf{D}}(\mathbf{k})\right\|^2\right]$ is the mean square error (MSE) in the estimation, where $E(\cdot)$ is denoted as the expectation operation.

Since for a not very large scene, spatially statistics stationary is generally satisfied, after some manipulations, ξ can be written as

$$\begin{aligned} \xi = \sum_{j=1}^{4} P_{D_j}\left(\mathbf{k}\right) &- 2\sum_{j=1}^{4}\sum_{i=1}^{4} P_{D_j}\left(\mathbf{k}\right) H_{ij} W_{ji}^{*}\left(\mathbf{k}\right) \\ &+ \sum_{j=1}^{4}\sum_{i=1}^{4}\sum_{m=1}^{4} W_{ji}\left(\mathbf{k}\right) P_{\Phi_{im}}\left(\mathbf{k}\right) W_{jm}^{*}\left(\mathbf{k}\right), \end{aligned} \tag{11}$$

where P_{D_j} is the PSD of the estimation parameter, W is the coefficient element in the MWF, H_{ij} are the elements of the observation matrix,

$$P_{\Phi_{im}}\left(\mathbf{k}\right) = \mathbf{H_i}\mathbf{R_{P_D}}(\mathbf{k})\mathbf{H_m^H} + P_N\left(\mathbf{k}\right) \tag{12}$$

is the cross-spectral matrix of the D-InSAR interferometric phases and $\mathbf{H_i}$ and $\mathbf{H_m}$ are the ith and mth row vectors of the observation matrix $\mathbf{H}$, respectively. In the right hand of (12),

$$\mathbf{R_{P_D}}(\mathbf{k}) = \begin{pmatrix} P_{D_{los}}(\mathbf{k}) & P_{D_{los}D_a}(\mathbf{k}) & P_{D_{los}D_p}(\mathbf{k}) & P_{D_{los}D_{atm}}(\mathbf{k}) \\ P_{D_aD_{los}}(\mathbf{k}) & P_{D_a}(\mathbf{k}) & P_{D_aD_p}(\mathbf{k}) & P_{D_aD_{atm}}(\mathbf{k}) \\ P_{D_pD_{los}}(\mathbf{k}) & P_{D_pD_a}(\mathbf{k}) & P_{D_p}(\mathbf{k}) & P_{D_pD_{atm}}(\mathbf{k}) \\ P_{D_{atm}D_{los}}(\mathbf{k}) & P_{D_{atm}D_a}(\mathbf{k}) & P_{D_{atm}D_p}(\mathbf{k}) & P_{D_{atm}}(\mathbf{k}) \end{pmatrix}, \tag{13}$$

is the cross-spectral matrix of $\boldsymbol{D}$, with $P_{D_{los}}$, P_{D_a}, P_{D_p}, and $P_{D_{atm}}$ the PSDs of deformations in the LOS, azimuth, their cross product direction, and the zenith DTD. The off-diagonal elements in (13) are the corresponding cross-spectra of the parameters. P_N is the PSD of noise, which is contributed by the terms described in equation (3).

Generally, the solution of (10) can be determined by setting the gradient of the object function with respect to the filter parameters to zero, namely,

$$\mathbf{W}\left(\mathbf{k}\right), s.t. \frac{d\xi}{dW_{ji}\left(\mathbf{k}\right)} = 0, i, j = 1, 2, 3, 4, \tag{14}$$

Based on the obtained gradient equations, assuming each parameter in $\mathbf{D}(\mathbf{k})$ is independent with respect to the others, we

can finally obtain the coefficients of the MWF in wavenumber domain as

$$
\begin{aligned}
W_{ji}\left(\mathbf{k}\right) = & \frac{P_{D_j}(\mathbf{k})H_{ij}}{P_{\Phi_{ij}}(\mathbf{k})} - \\
& \frac{\sum\limits_{n=1, n\neq i}^{4} P_{\Phi_{in}}(\mathbf{k})W_{jn}{}^{*}(\mathbf{k})}{2P_{\Phi_{ij}}(\mathbf{k})} - \\
& \frac{\sum\limits_{m=1, m\neq i}^{4} W_{jm}(\mathbf{k})P_{\Phi_{mi}}(\mathbf{k})}{2P_{\Phi_{ij}}(\mathbf{k})} \\
& , i, j = 1, 2, 3, 4.
\end{aligned}
\tag{15}
$$

Written in a compacted form, for each channel-group in MWF, (15) is given by

$$
\mathbf{W}_i(\mathbf{k}) = \left\{[U_i\left(\mathbf{H}\right) \odot \mathbf{R_{P_D}} \odot V_i\left(\mathbf{H}\right)] + \mathbf{P_N}\left(\mathbf{k}\right)\right\}^{-1}\mathbf{H}_i^H \odot \mathbf{P_{D_r},i}\left(\mathbf{k}\right),
$$
$$
i = 1, 2, 3, 4,
\tag{16}
$$

where $\mathbf{P_{D_r},i}(\mathbf{k})$ is the row vector of $\mathbf{P_{D_r}}(\mathbf{k})$,

$$
\mathbf{P_{D_r}} = \begin{pmatrix}
P_{D_{los}}(\mathbf{k}) & P_{D_{los}}(\mathbf{k}) & P_{D_{los}}(\mathbf{k}) & P_{D_{los}}(\mathbf{k}) \\
P_{D_a}(\mathbf{k}) & P_{D_a}(\mathbf{k}) & P_{D_a}(\mathbf{k}) & P_{D_a}(\mathbf{k}) \\
P_{D_p}(\mathbf{k}) & P_{D_p}(\mathbf{k}) & P_{D_p}(\mathbf{k}) & P_{D_p}(\mathbf{k}) \\
P_{D_{atm}}(\mathbf{k}) & P_{D_{atm}}(\mathbf{k}) & P_{D_{atm}}(\mathbf{k}) & P_{D_{atm}}(\mathbf{k})
\end{pmatrix},
\tag{17}
$$

$U_i(.)$ and $V_i(.)$ are transfer matrices where each element is a 4 by 4 block matrix relating to $\mathbf{H_i}$, and $\odot$ represents Hadamard product of block matrix.

The estimation accuracy of the ith element in $\hat{\mathbf{D}}$ can be expressed by

$$
\begin{aligned}
\sigma_{e,i} &= \left[\iint E\left\{[D_i\left(\mathbf{k}\right) - \mathbf{W}\left(\mathbf{k}\right)\mathbf{\Phi}\left(\mathbf{k}\right)][D_i\left(\mathbf{k}\right) - \mathbf{W}\left(\mathbf{k}\right)\mathbf{\Phi}\left(\mathbf{k}\right)]^{*}\right\}d\mathbf{k}\right]^{1/2} \\
&= \left[\iint\left\{P_{D_i} - 2\mathbf{M_{P_D}}\mathbf{H}\mathbf{G}_i^H(\mathbf{k}) + \mathbf{G}_i(\mathbf{k})\mathbf{H}\mathbf{R_{P_D}}\mathbf{H}^H\mathbf{G}_i^H(\mathbf{k})\right\}d\mathbf{k}\right]^{1/2},
\end{aligned}
\tag{18}
$$

where

$$
\mathbf{M_{P_D}} = \left[P_{D_{ij}}, P_{D_{ik}}, P_{D_{im}}, P_{D_{in}}\right], i, j, k, m, n = 1, 2, 3, 4,
\tag{19}
$$

$$
\mathbf{G_i}(\mathbf{k}) = \frac{\mathbf{H}_i^H}{[U_i\left(\mathbf{H}\right) \odot \mathbf{R_{P_D}} \odot V_i\left(\mathbf{H}\right)] \odot \mathbf{P_{Dr},i}^{-1} + \mathbf{SNR_i}^{-1}},
\tag{20}
$$

$\mathbf{SNR_i}$ is the signal-to-noise ratio vector of the ith element in $\hat{\mathbf{D}}$ with respect to the noise in the interferograms. Like the single-channel Wiener filter [31]–[33], the estimation accuracy also depends on $\mathbf{SNR}$, where the filtering is conducted adaptively to the quality of the signal. When the SNR tends to infinite, $\sigma_{e,i}$ goes to zero; otherwise, it tends to the variance of $\mathbf{d}$.

Finally, the joint estimation of the multi-dimensional deformation and the DTD can be realized optimally based on the statistical characteristics of these estimated parameters in the MWF-based method. Prior knowledge of deformations in the monitoring region can be acquired from historical recorded data, in-situ measurements, global navigation satellite system (GNSS) data, and some strain models. A prior DTD knowledge can be determined from InSAR data patch in the deformation-free areas in the region or from the non-overlapped spatial frequency region of deformations and DTD in the interferogram's PSDs [34]. In addition, prior knowledge can also be generally estimated from an initial FRI processing. The estimation of PSDs of phase noise components is also
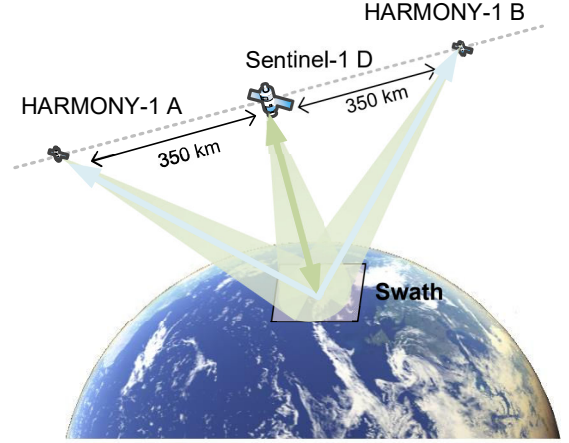

Fig. 3. Sketch map of the Harmony multi-angle spatial observation.

not sophisticated. The thermal phase noise PSD energy can generally be calculated using (4) and the interferogram's estimated coherence. The PSD of the DTD decorrelation phase component can be estimated by (7) with the prior DTD knowledge, and the baseline error part and residual ionospheric part can be obtained through classical orbit error models and ionospheric phase spectra.

IV. VALIDATION AND DISCUSSION

A. Simulation validation and performance analysis

Harmony multistatic SAR system represents a forthcoming simultaneous spaceborne multi-angle SAR, which is the ESA EE-10 mission candidate and entered into the Phase B1 stage in 2022. The system includes the mono-static Sentinel-1 D SAR, the only active satellite, and two receive-only bistatic Harmony satellites. As shown in Fig. 3, the passive satellites distributed about 350 km ahead and behind the active satellite (inter-satellite distance). In this section, we take the Harmony system as an example of simultaneous spaceborne multi-angle SAR to validate the proposed method, where Table I provides the simulation parameters. The Harmony system acquires three observations simultaneously, but with the three effective LOS vectors approximately contained in a 2-D plane. Consequently, we can use the resulting InSAR data to estimate two deformation components (the LOS direction of the reference satellite and its azimuth direction) and the DTD.

The interferometric phase of deformations, DTDs, thermal noise, residual ionospheric phases, and baseline errors are simulated and included to generate the D-InSAR interferograms of the Harmony system. The reference LOS and azimuth deformations and the zenith DTD are shown in Fig. 4 (a)-(c). We use Mogi Point-source model to generate 2-D deformations aligned with Sentinel-1's imaging geometry [35], where the simulation parameters are given in Tab. II. The reference zenith DTD is generated based on Kolmogorov's power-law spectrum with a standard deviation of 1.5 rad and a spectral index of -5/3 [3]. Then, projected to each LOS directions of the different satellites in the Harmony system, the mapped DTD phases are simulated, where the uncorrelated DTD components

TABLE I
PARAMETERS OF THE HARMONY SYSTEM AND THE ASSUMED ERROR IN
THE SIMULATIONS

Parameters	Value
Carrier frequency (GHz)	5.405
Orbit altitude (km)	693
Bandwidth (MHz)	50
Inter satellite distance (km)	350
Scene size (km)	50
Pixel size (m)	100
Look	100
Turbulence model spectral index	Power-law/-5/3
Troposphere height (km)	2
CkL Rino spectral indel	30/3
Averaging scale in split spectrum (km)	50
Absolute baseline accuracy (1σ) (cm)	7
Relative baseline accuracy (1σ) (mm)	1

TABLE II
SIMULATION PARAMETERS OF THE DEFORMATIONS AND UTILIZED MODEL
PARAMETERS TO ESTIMATE THE PSDs IN THE MWF.

Parameters	Real value	Model value
DTD turbulence (1σ) (rad)	1.50	1.58
X direction of the displacement point pressure source (m)	0	10
Y direction of the displacement point pressure source (m)	0	10
Depth of the displacement point pressure source (km)	10	10.01
Changed volume ($10^6 m^3$)	50	51
Poisson's ratio	0.25	0.25

TABLE III
PROCESSING ERROR EVALUATION

Deformation accuracy (RMSE)	Los (mm)	Azimuth (mm)	DTD (mm)
Case 1 (FRI)	77.89	22.88	70.41
Case 1 (FRI, 50 × 50 boxcar filtering)	5.64	2.76	7.48
Case 1 (MWF)	1.93	1.67	1.78
Case 2 (MWF)	4.55	2.33	4.14

are automatically included according to different observation geometries of the Harmony satellites. The thermal noise is simulated according to (4), assuming a coherence of 0.8 and the number of looks listed in Table I. Applying (5) and the parameters in Table I, the residual phases from high-frequency ionospheric components are simulated based on the Rino spectrum [36]. Baseline phase errors in the Harmony's interferograms are included according to the parameters in Table I.

Two simulation cases are studied with different distances between each Harmony satellite and Sentinel-1 D: 1) 350 km and 2) 50 km. The joint retrieval results of 2D deformation and DTDs in two cases with different processing methods and parameters are shown in Fig. 4. The corresponding estimation accuracy based on Root Mean Square Error (RMSE) is given in Table III. Fig. 4 (d)-(i) are the estimation results by the FRI method, while Fig. 4 (j)-(r) are the retrieved results by the proposed MWF method. We assume that the utilized model parameters to estimate the required PSDs in the MWF have some errors which are shown in Tab. II.

First of all, these results demonstrate that a multi-angle

D-InSAR system like the Harmony has the capability to retrieve both the multi-dimensional deformations and the DTDs. Nevertheless, different methods perform differently. The FRI obtains very noisy results, where there are lots of high-frequency residual components from DTD decorrelation phases, as shown in Fig. 4 (d)-(f). The estimation accuracy is compromised, with results in the order of several centimeters, resulting in considerably blurred deformations. When applying a 50 × 50 box moving averaging before the FRI, the estimated spatial low-frequency deformation turns clear and the accuracy improves in Fig. 4 (g)-(i). Logically, after the spatial averaging, all the shorter wavelength components are missing in the estimated DTD. Meanwhile, it should be noted that there is a constant spatial frequency error in the FRI inversion results, where its wavenumber along the ground-range direction is about $7 \cdot 10e^{-5} m^{-1}$ (3.5 cycle / 50 km). The cyan lines in in Fig. 5 (b) provides a spatial wavenumber spectral analysis of the phase errors in the interferogram at the ground-range direction. The spatial wavenumber component producing the constant spatial frequency error is marked by the arrow, which mainly comes from the residual ionospheric phase error. In contrast, MWF can clearly recover the detailed features of the deformation signals and the DTD, where the accuracy improves. Some detailed features are marked as white boxes in Fig. 4 for comparison. The main cause for estimation error in the MWF approach is the coupling between the deformation and the DTD in the low-frequency domain, which could be seen from the DTD estimation error map in Fig. 5 (a). This coupling appears because the long wavelength spectral components of the DTD overlap in the wavenumber domain with the deformation signal, as shown by the gray and blue lines in Fig. 5 (b). At such low-frequency wavenumbers, baseline errors and residual ionospheric phase errors in interferograms have large energy, as indicated by the pink line. As a result, SNR reduces, as discussed in Session II, and therefore DTD and deformations can only be decoupled with degraded accuracy. At other wavenumbers, comparing the blue, red, and cyan lines, the spectra of the estimated DTD and the reference one are very alike, which suggests that MWF can map relatively small-scale DTD spatial features in this case. Nevertheless, the constant spatial frequency error observed in the estimated deformations by FRI is not evident in the MWF results. Since the studied deformation mainly has the spatial wavenumber components lower than $7 \cdot 10e^{-5} m^{-1}$ (see gray lines in Fig. 5 (b)), the spatial periodical errors are filtered out when estimating deformations in the MWF inversion.

As expected, we observe that the performance in Case 1, characterized by a longer separation between satellites, is somewhat superior to that observed in Case 2. This is further examined in Fig. 6, which shows the estimation performance of multi-dimensional deformations and DTDs as functions of inter-satellite distance. The performances are studied based on the statistical analyses of RMSEs from 100 repeat experiments with random interferometric phase errors, DTDs, and deformations. The random deformations in the repeat experiments are generated according to the truth-value parameters in Tab. II with a 10 m standard deviation in 3-D positioning and a 1000 m^3 standard deviation of volume change. In the MWF
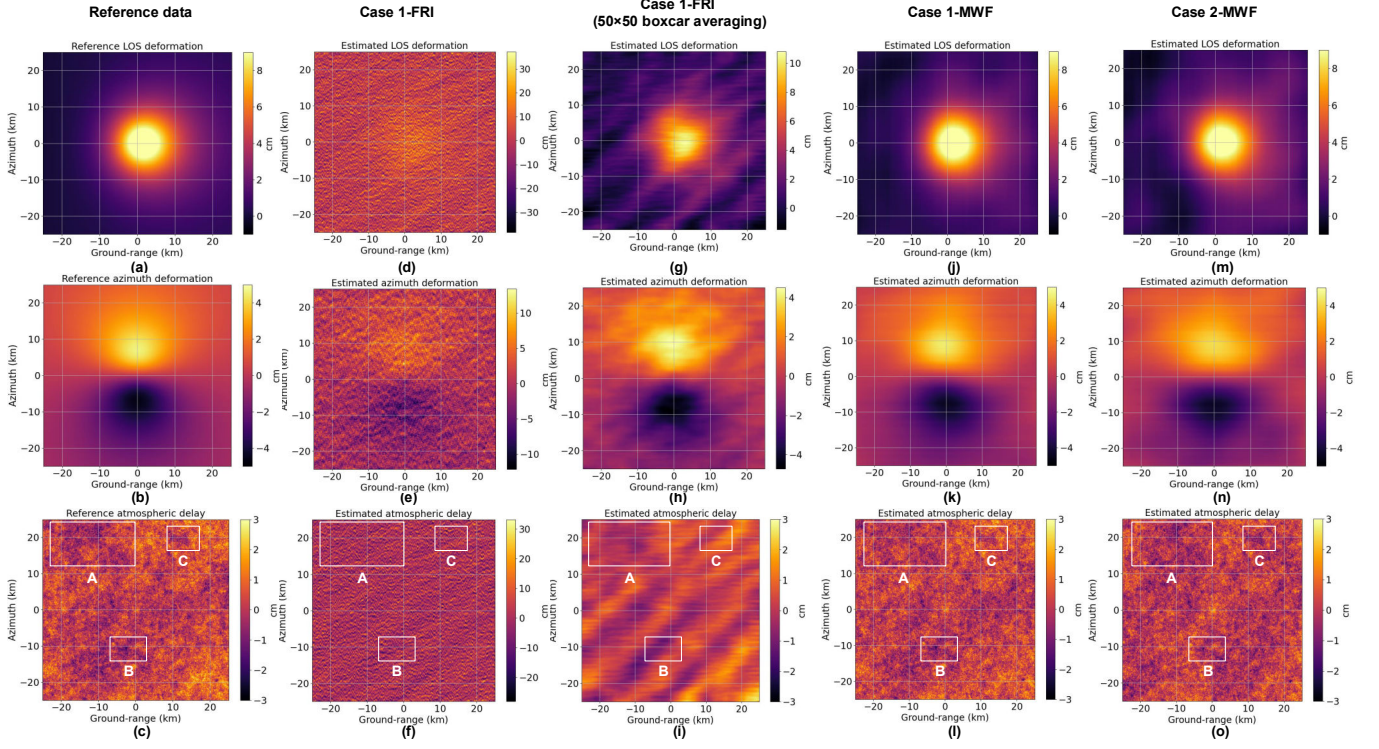
Fig. 4. Deformations and DTDs. Reference data: (a) LOS deformation; (b) azimuth deformation; (c) DTD. By FRI in Case 1: (d) LOS deformation; (e) azimuth deformation; (f) DTD. By FRI with 50×50 boxcar averaging in Case 1: (g) LOS deformation; (h) azimuth deformation; (i) DTD. By MWF processing in Case 1: (j) LOS deformation; (k) azimuth deformation; (l) DTD. By MWF processing in Case 2: (m) LOS deformation; (n) azimuth deformation; (o) DTD. The white boxes in the figures indicate some typical details in DTDs.
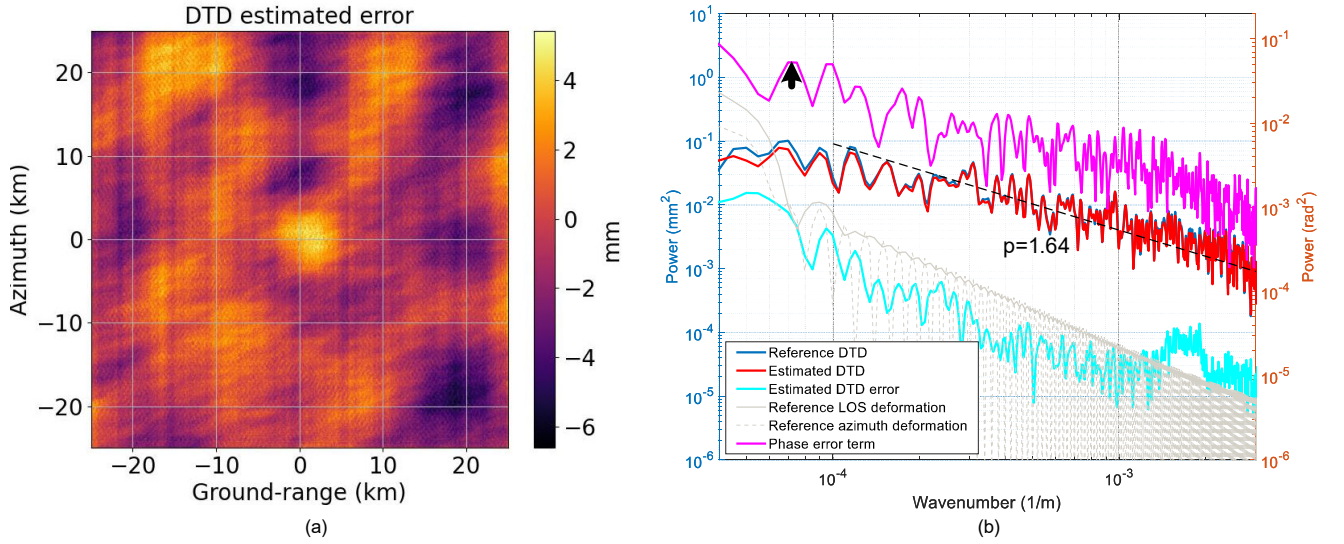
Fig. 5. DTD estimation error in Case 1 (a) and the analysis of its PSD (b). The PSD are estimated at $ky = 0$ (azimuth direction) as function of kx (ground-range direction). We take the phase error term in the Harmony 1-A's interferogram as an example. The arrow in the figure (b) indicates the spatial wavenumber component of the interferometric phase error to generate the constant spatial frequency errors in the FRI results in Fig. 4

processing, we also consider the same amount of model errors when estimating the PSDs of deformations. The reference DTDs have a standard deviation of 1.5 rad, while a nearly 1.6 rad standard deviation of DTDs is used to simulate DTD model error in the MWF processing. The interferometric phase errors φ_n simulated by the parameters in Tab. I are also considered
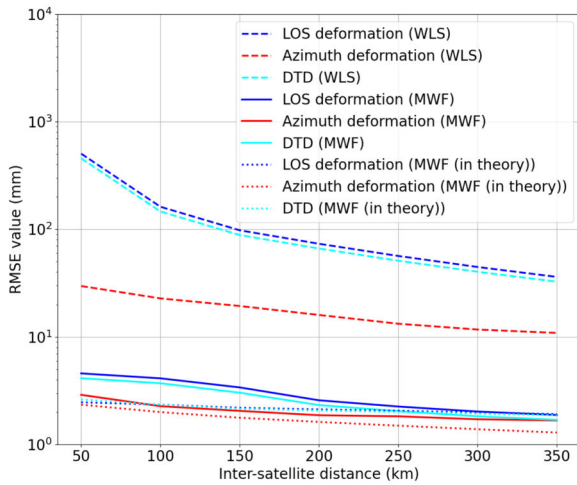
Fig. 6. RMSE analyses of the estimated multi-dimensional deformations and DTDs as functions of inter-satellite distance. The considered errors in the D-InSAR interferograms and the processing parameters are given in Tab. I. The errors between the utilized model parameters to estimate the required PSDs and their truth-values are listed in Tab. II

in the analysis. The results show that MWF can achieve better estimation accuracy compared to the FRI under different inter-satellite distances. In Case I, the estimation RMSEs of deformations and DTDs using MWF are only less than 2 mm. In contrast, accuracy worsens by factors ranging from 6 to more than 10 times in the FRI, suggesting FRI is very sensitive to errors. Fig. 6 also show that the accuracy improves with the increase of the distance between satellites. Larger spatial separations between satellites offer a better observation diversity, which can reduce the sensitivity of the system to noise. Nevertheless, MWF is quite robust to the change of inter-satellite distance. Since a larger filtering window will be automatically applied in the MWF method under a small distance case, the estimation accuracy does not change significantly when the distance increases. For both two methods, it can be seen that curves become flattened at an inter-satellite distance of approximately 300 km because DTD decorrelation phases progressively turn larger. Therefore, a longer separation between the satellites will not bring many benefits but can raise the complexity of the system. The estimation is suitable for a simultaneous multi-angle SAR like the Harmony system, which can both offer enough spatial observation diversity and keep the observed DTD from different satellites largely correlated. Finally, note that the performance achieved with the Monte Carlo simulation matches well the predicted theoretical performance as given by (18).

From the above analysis, we can conclude that there are large inversion coupling errors between the estimated LOS deformation and the DTD in the FRI joint inversion, especially when the inter-satellite distance is not large. Since deformations are more interesting for us in Case 1, we can only estimate LOS and azimuth deformations to improve the estimation accuracy by reducing the number of parameters to

be estimated. The corresponding results are shown in Fig. 7 (a)-(d). The estimation RMSEs of deformations are reduced in both with and without boxcar filtering cases. There is no large coupling error in the estimated LOS deformation, the RMSE is 6.64 mm, which is almost equivalent to the RMSE of the DTD (6.6 mm). Similar conclusions can be drawn for different inter-satellite cases, as evident from the comparison between Fig. 7 (e) and Fig. 6. When only inverting deformations by FRI, the error in LOS is almost independent of the along-track distance, while the deformation error along azimuth is about a factor 2-6 worse. It suggests that even though the system has the capability to jointly estimate both deformations and DTD the FRI cannot achieve a satisfactory result when more parameters need to be estimated. Under this case, the MWF method also performs better, which shows the significance of improving deformation estimation accuracy by using multi-angle InSAR to separate DTD. In fact, it is of importance for the small surface deformation estimation cases (millimeter-level), where tiny deformation will be covered when regardless of DTD. To simulate a simple case for it, we only change the changed volume in the point pressure source displacement model in Case 1 to $15e^6 \text{m}^3$, then the generated deformation becomes small as shown in Fig. 8 (a) and (b). The estimated results by MWF and FRI (without inverting DTD and with boxcar filtering) are given in Fig. 8 (c)-(f) respectively. By MWF-based method, the LOS deformation does not show many DTD features and its azimuth deformation can reserve the deformation pattern, while the DTD component severely distorts the deformations in the FRI results. It indicates the effectiveness of the MWF method for small deformation retrieval in the presence of DTD.

B. Real-data study: TanDEM-X bidirectional SAR cases in California, USA

TanDEM-X is an interferometric SAR system consisting of two SAR satellites flying in close formation [37]. Among the different experiments that have been conducted with TanDEM-X [38], the bidirectional SAR (BiDi SAR) mode [29] stands out for enhancing azimuth deformation estimation accuracy. In this mode, the system achieves symmetrical imaging of two directions using one antenna at the same time, greatly increasing the angular diversity, i.e., the scene is observed under two different squint angles within the same acquisition. In the BiDi SAR mode experiment presented in this paper, as illustrated in Fig. 9, one satellite (TDX) makes an acquisition over the scene in the conventional zero-Doppler stripmap mode, while the second satellite (TSX) makes an acquisition over the same area with the BiDi mode, which hence results in 3 LOS observations. All satellites operate in monostatic mode and both the forward-looking and backward-looking antenna squint angles in the TSX are about $2.2°$.

As for the joint estimation, two important differences between the TanDEM-X BiDi SAR and the simultaneous multi-angle SAR should be noted. First, since the TanDEM-X BiDi SAR images three different scenes simultaneously, the acquisitions of the same scene in different LOS directions have time lags of several seconds, which gives rise to additional
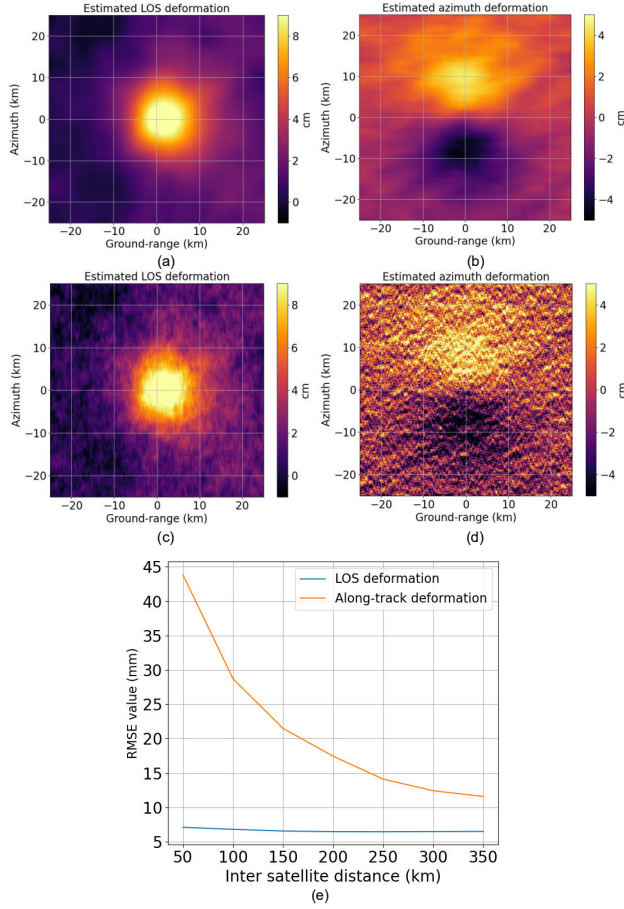
Fig. 7. The retrieved LOS deformation (a) and azimuth deformation (b) by FRI in Case 1 by just estimating the deformation without inverting the DTD (boxcar filtering) (LOS deformation RMSE: 4.69 mm, azimuth deformation RMSE: 2.76 mm). (c) and (d)are corresponding retrieved deformations without boxcar filtering (LOS deformation RMSE: 6.64 mm, azimuth deformation RMSE: 22.88 mm). (e) RMSE analyses of the estimated multi-dimensional deformations as functions of inter-satellite distance by FRI (without boxcar averaging, by the statistical analyses of deformation RMSEs by 100 repeat experiments). The considered errors in the D-InSAR interferograms and the processing parameters are given in Tab. I.
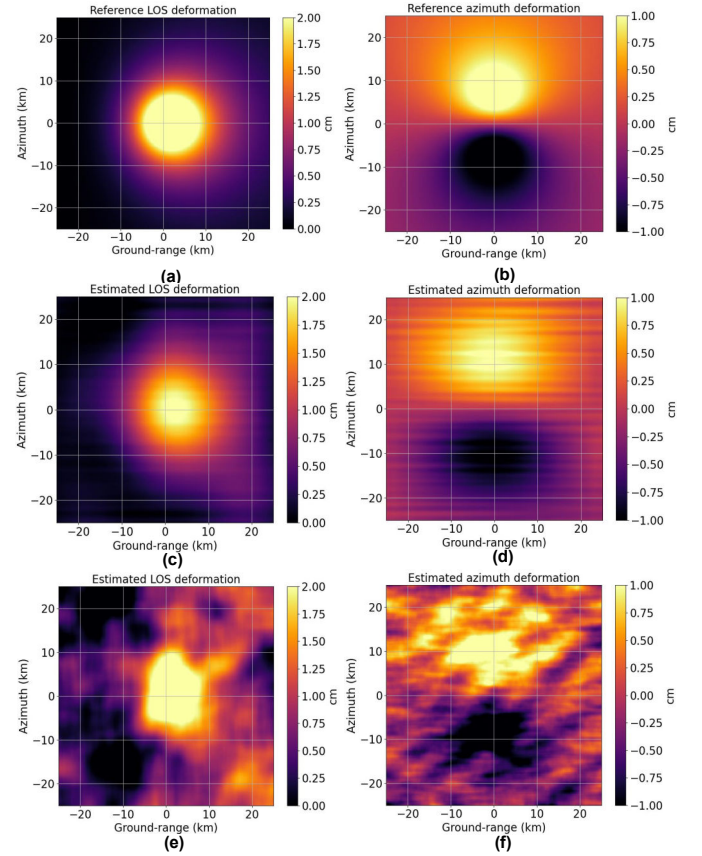

Fig. 8. Reference LOS deformation (a) and azimuth deformation (b). Estimated deformations by WMF: (c) LOS deformation (RMSE: 2.13 mm); (d) azimuth deformation (RMSE: 1.26 mm). Estimated deformations by FRI (without inverting DTD; with 50 × 50 boxcar filtering): (e) LOS deformation (RMSE: 4.56 mm); (f) azimuth deformation (RMSE: 2.69 mm).

DTD decorrelation phases between interferograms, mainly due to advection and possible shear within the troposphere. In addition, note that the BiDi SAR imaging mode provides a limited geometry diversity, which would correspond to an observation diversity of two Harmony satellites separated about 30 km in the along-track direction. In spite of these differences, multi-angle observation with a few seconds time lags offers the opportunity to verify our proposed method to some extend.

We select two experiment scenes with different terrains in California, USA. One scene is a nearly $9km \times 11km$ flat area close to Fountain Valley, which is shown by the red rectangle A in Fig. 10 (a). The other scene is an approximately $13km \times 17km$ region including rugged mountains (about 800 m elevation variation) near the Desert Tortoise Natural Area, as shown by the red rectangle B in Fig. 10 (b). The elevation variations of two scenes from SRTM 30 digital elevation
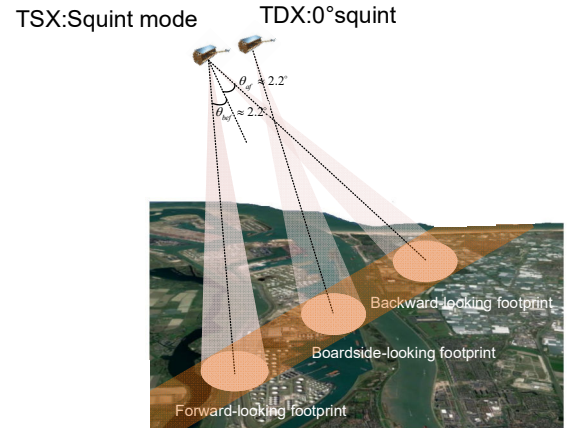

Fig. 9. Acquisition geometry of the TanDEM-X BiDi SAR imaging mode.

model (DEM) are provided in Fig. 10 (c) and (d), respectively. The InSAR pairs of both two scenes were acquired by the TanDEM-X ascending tracks on 7th and 18th December 2019. A small repeat time interval is chosen so that we can assume
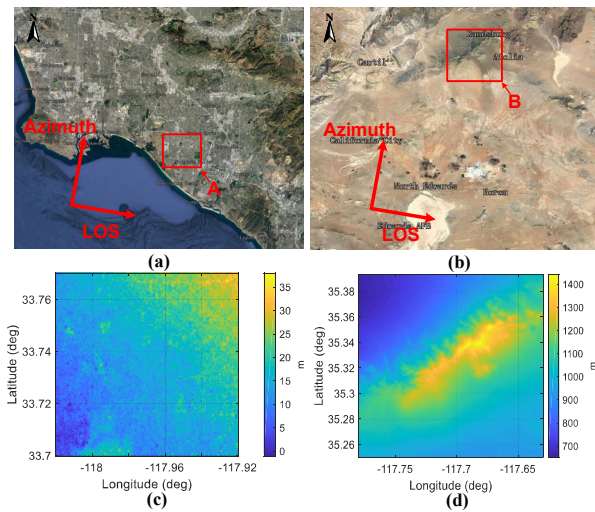
Fig. 10. Data acquisition scene and geometry of our experiment. (a) flat area case; (b) rugged terrain case; (c) DEM of the flat area scene; (d) DEM of the rugged terrain scene. The experiment scene is marked as the red rectangle in figures.

that the main D-InSAR phases are DTD phases.

1) Flat area case: For the flat area case, its primary images (7th December 2019) of three LOS directions are shown in Fig. 11 (a)-(c). Three interferograms after coregistration and calibration based on high-coherence points in the area are shown in Fig. 11 (d)-(f). According to the United States Geological Survey (USGS) Earthquake Hazards Program, there were no obvious earthquakes near our scene during the experiment period (See Appendix A). In addition, the time interval between acquisitions is only 11 days. Therefore, we can consider that the D-InSAR phases in the three interferograms are mainly DTD phases. Many similar texture features from water vapor variations can be seen in these D-InSAR interferograms.The motion of the DTDs in three interferograms within the time lags of TanDEM-X BiDi SAR mode can be partially mitigated by coregistration.

When conducting the MWF processing, the DTD in spatial is modelled by a power-law spectrum with an index of -5/3 and its intensity can be computed based on the phase variation in the interferogram. For the power spectra of the deformations in the scene, we draw upon a prior information in the region. The scene is situated within the $20km \times 40km$ Santa Ana basin. This region has been subject to subsidence attributed to groundwater pumping and oil extraction (see Appendix A). Bawden et al. [39] showed that the net annual subsidence along a 60 km profile cross the basin is a spatial low-frequency signal and its amplitude is about 16 mm per year. Thus, combing the above prior information of the deformation in the scene, to estimate the spatial power spectra we assume that the deformations in all directions are statistical homogeneously with a standard deviation of 0.08 mm from the subsidence during the experiment period (assumed that it is a temporal and spatial linear accumulated deformation all projected to the LOS of radar observation with a spatial correlation distance of 30 km (average length of the basin)). After the coregistration

and calibration of the interferograms, the differences between them are considered to be the residual DTD decorrelation phases from vertical mixing during the time lags and phase noise. The spectra of these residual phases are calculated and added into $\mathbf{P_{N_{ik}}}$ in (12).

The estimation results of the LOS deformation, the azimuth deformation, and the DTDs by MWF are shown in Fig. 12 (c)-(e). For comparison, since the spatial diversity in TanDEM-X BiDi SAR case is limited, the FRI results with only the inversion of deformations are provided in Fig. 12 (a) and (b). It can be seen that the estimated deformations by FRI are quite large, which are about 10 cm in azimuth and 1-2 cm in LOS. Because the DTD can not be decoupled with LOS deformation, many DTD texture features are erroneously regarded as LOS deformation. At the same time, even though most coherent DTD is cancelled due to the symmetry of the forward- and backward-looking observations in azimuth, because of the poor spatial diversity of the system, the inversion of the FRI method for azimuth deformation is very sensitive to phase noise terms from such as DTD decorrelation phases, etc. [23]. In contrast, since we consider the a prior knowledge of the deformations and DTD in the MWF method, the estimated deformations are similar to the prior models we assumed, which is small and smooth during the InSAR acquisition period, and the estimated DTD has a low noise level while also preserving the high-resolution details. As shown in Fig. 13 (a), the spatial PSD of the estimated DTD in the longitude direction follows a power-law behavior with a spectral index of about -1.7, which approaches the spectral law assumed for the implementation of the MWF estimator. Furthermore, given our assumption that the majority of interferometric phases correspond to DTD, we present a comparison between the retrieved DTD using the MWF approach and a single phase signal derived from TDX. This comparison is illustrated in Fig. 13 (b) and (c). Compared to the results with Fig. 12 (e), the DTD retrieved by MWF is quite similar to that directly estimated from the single phase signal of TDX, with a reduced range of the DTD variation and an root mean square value of 1.94 mm.

2) Rugged terrain case: By the same processing procedures, we jointly estimate deformations and DTD by the TanDEM-X BiDi InSAR pairs of the Rugged terrain case. The corresponding three SAR images obtained on 7th December 2019 and the generated D-InSAR interferograms fter coregistration and calibration are shown in Fig. 14. In this case, because of the obvious elevation changes in the scene, obvious DTD fringes in the D-InSAR interferograms are from atmospheric stratification effects.

In the MWF processing, similarly, we model the spatial PSDs of both deformations and DTD. According to the Appendix, the scene is not a subsidence and landslide area and is also free of intense earthquakes between two acquisitions of the InSAR pair. Considering the short temporal baseline of the InSAR pair, we assume that the deformations are statistically homogeneous in space with a standard deviation of 1 mm and a spatial correlation distance of 10 km, which may derive from some unpredictable deformation sources or several weak earthquakes. Since the DTD in the rugged terrain
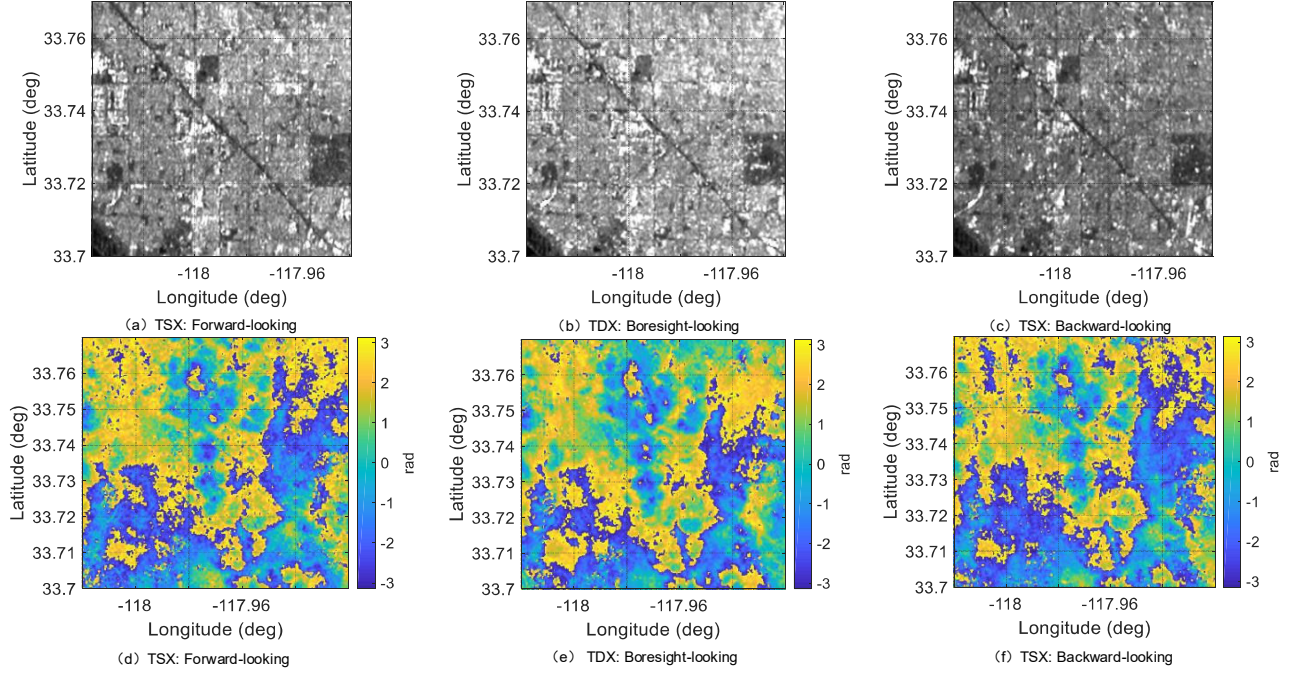
Fig. 11. The TanDEM-X SAR primary images (7th December 2019) and the corresponding generated D-InSAR interferograms after coregistration and calibration of the flat area case. (a) Forward-looking image of TSX; (b) Boresight-looking image of TDX; (c) Backward-looking image of TSX; (d) Forward-looking D-InSAR interferogram of TSX; (e) Boresight-looking D-InSAR interferogram of TDX; (f) Backward-looking D-InSAR interferogram of TSX.
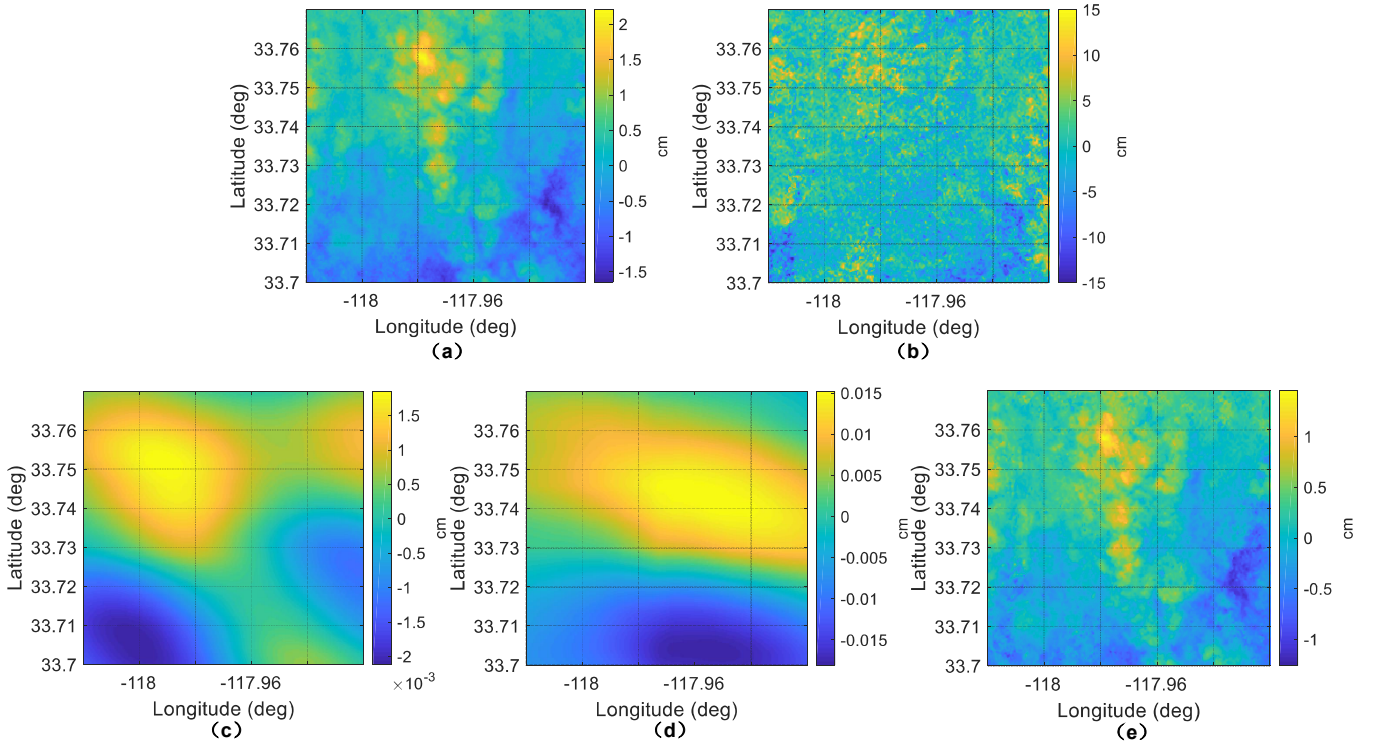

Fig. 12. Joint estimation results of the flat area case by the FRI with only inverting deformations and the proposed MWF-based method. FRI: (a) LOS deformation; (b) azimuth deformation. MWF-based method: (c) LOS deformation; (d) azimuth deformation; (e) DTD.
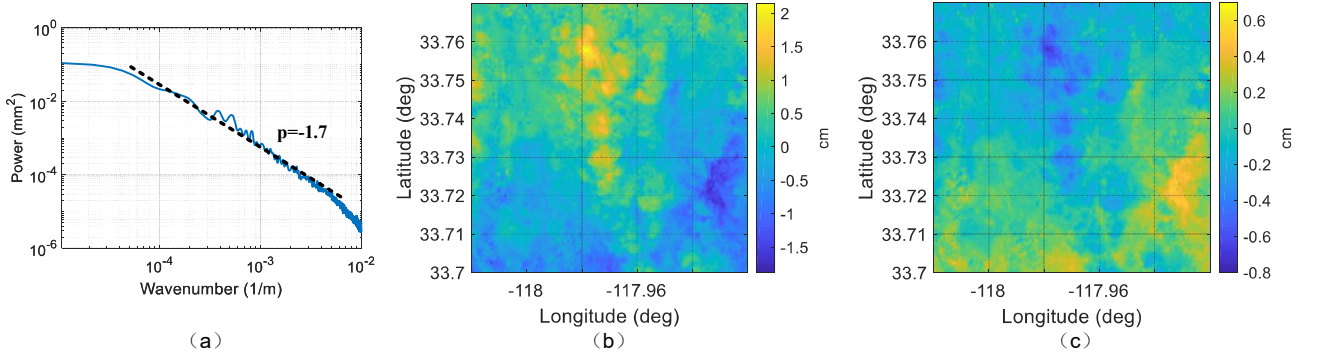
Fig. 13. Performance evaluation of the estimated DTD by MWF. (a) PSD of the DTD by the MWF-based method. The PSD are estimated at $ky = 0$ (latitude direction) as function of kx (longitude direction). The dashed black line indicates the fitted power-law spectrum of DTD and p is the corresponding spectral index. (b) DTD estimated from a single phase signal of the TDX acquisition and (c) the difference of the DTDs between estimated DTD by MWF and (b). The root mean square value of (c) is 1.94 mm.)
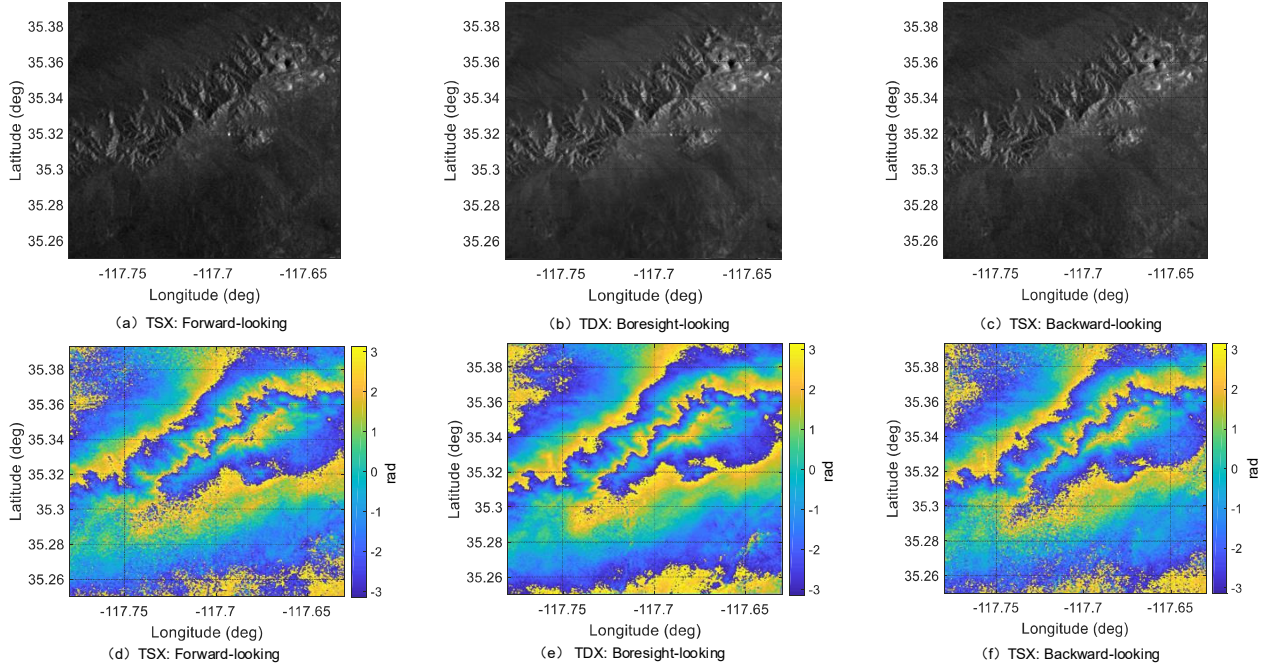

Fig. 14. The TanDEM-X SAR primary images (7th December 2019) and the corresponding generated D-InSAR interferograms of the rugged terrain case. (a) Forward-looking image of TSX; (b) Boresight-looking image of TDX; (c) Backward-looking image of TSX. D-InSAR interferograms after coregistration and calibration: (d) Forward-looking D-InSAR interferogram of TSX; (e) Boresight-looking D-InSAR interferogram of TDX; (f) Backward-looking D-InSAR interferogram of TSX.

case is almost from the atmospheric stratification effects, an atmospheric turbulence PSD is no longer applied. Generally, DTD from atmospheric stratification has a strong spatial correlation with the topography [40]. Thus, we use the spatial PSD model of the topography to model the PSD of DTD in space. It is well known that the topography of the Earth shows fractal properties and its spatial PSD can be modelled by a power-law spectrum [41]. As shown by the red line in Fig.15 (f), the slope of the PSD of the scene elevation variation is

about -1.72, which we take as the paw-law spectrum index to model the PSD of DTD. The integral PSD power of the DTD can also be estimated based on the phase variation in the interferogram because of the dominance phases from DTD in the interferograms. Other PSDs of interferometric phase errors are estimated by the same method that is used in the flat area case.

In Fig.15, (a), (c) and (e) show the estimation results of LOS deformation, azimuth deformation, and DTD by the MWF method in the rugged terrain case. Fig.15 (b) and
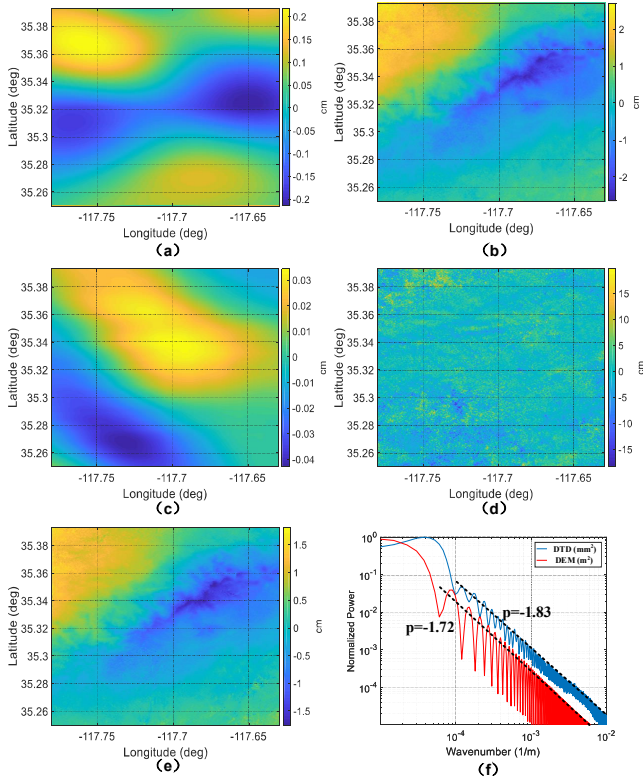
Fig. 15. Joint estimation results of the rugged terrain case by the MWF method and the FRI with only inverting deformations. (a) estimated LOS deformation by MWF method; (b) estimated LOS deformation by FRI; (c) estimated azimuth deformation by the MWF method; (d) estimated azimuth deformation by FRI; (e) estimated DTD by the MWF method; (f) PSDs of the estimated DTD and DEM of the scene. he PSD are estimated at $ky = 0$ (latitude direction) as function of kx (longitude direction). The dashed black line indicates the fitted power-law spectrum of DTD and p is the corresponding spectral index.

(d) are the estimation results of LOS deformation, azimuth deformation by FRI with only inverting deformations. Based on our previous deformation analysis of the scene, there is no obvious deformations during our InSAR acquisition. Because the prior knowledge of the spatial PSD are fused in the MWF estimation, the estimated LOS and azimuth deformations are less than 2 mm and show spatially correlated at a scale of about 10 km, which is consistent with the deformation condition of the scene. The estimated LOS deformation by the MWF method is also decoupled with DTD. DTD with many details is well estimated in Fig.15 (e). Its spatial PSD at the longitude direction is shown by the blue line in Fig.15 (f). The slope of the estimated PSD is about -1.83, which is almost consistent with the prior knowledge of the DTD PSD's slope. In contrast, being similar to the FRI estimation results of the flat area case, the estimation deformation results by FRI in this case also have large uncertainty because of the limited spatial diversity of TanDEM-X BiDi SAR. In Fig.15 (b), we can see almost all DTD components, which are the topography correlated pattern from atmospheric stratification delay, in the estimated LOS deformation by FRI. In the meantime, the estimated azimuth deformation ranges from several centimeters to more

than 10 cm, which is not in line with the prior knowledge of deformations in the scene.

Therefore, based on the experiment results of two different scenes using TanDEM-X BiDi SAR data, with the help of spatial statistical a prior knowledge of deformations and DTD, MWF can achieve much reasonable results even under limited spatial observation diversity and relatively large DTD decorrelated phases from non-simultaneous observations.

V. CONCLUSION

A simultaneous multi-angle SAR system has the capability to accurately obtain multi-dimensional deformations together with the DTD. The latter pollutes the deformation phases in single interferograms, and can only be mitigated with the exploitation of long time-series [11], [12]. In this study, we proposed an MWF-based method that optimally estimates multi-dimensional deformations alongside DTDs using simultaneous multi-angle D-InSAR data. By using a prior statistical knowledge to optimally filter each signal component from multiple noises, details in the scene and better accuracy are both achieved by MWF. The method has been verified by the simulations based on the parameters of the ESA EE-10 Harmony mission. The estimation performance has been analyzed under different inter-satellite distances with the consideration of multiple error sources.Compared to a FRI, which requires an intense spatial smoothing and a long inter-satellite distance to improve inversion accuracy, the MWF method achieves optimal filtering for each component and is robust to spatial observation geometry. Similar conclusions can also be derived based on the results obtained with the multi-angle TanDEM-X BiDi SAR data in both a flat area case and a rugged terrain case, which suggests that the proposed method will be helpful to retrieve small deformations.

It should be noted that some issues need to be specially considered to implement the method in the future. Geometrical distortions over different LOS interferograms in the rugged terrain scene should be corrected when the observation geometries of the satellites in the system are very different; otherwise, the estimation accuracy of the multi-dimensional deformation will degrade. Some DEM-assisted geocoding methods are possible ways, while reliable methods still need to be investigated to match the interferograms in mountain regions with very dramatic elevation variations. Moreover, using the proposed method requires prior knowledge of the deformations and DTD in the scene. Although external in-situ data, models, and initial estimation parameters from data can help provide some prior knowledge, in a scene with low-quality prior information, such as that with very complex deformation and atmospheric conditions, we will put our effort into finding alternative solutions. More experimental conditions and scenarios will be further studied to help ensure the accuracy of the method in different cases. At last, since the simultaneous multi-angle spaceborne system consists of multiple satellites, micro-satellites or Cubesats are promising platforms for the system. Nevertheless, several related fundamental techniques implemented on these small platforms, such as the small size and weight design of the radar payloads,
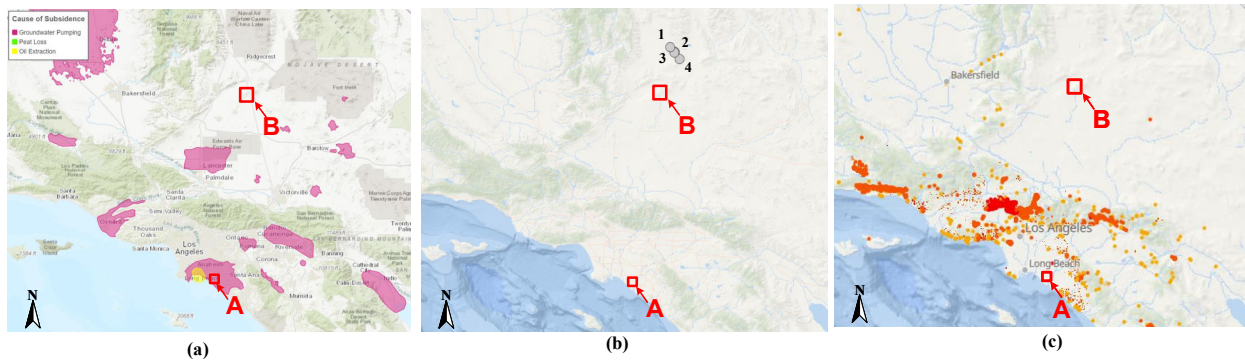
Fig. 16. Subsidence, earthquake activities, and landslides near the experiment scene. (a) Distribution of subsidence. The subsiding information is obtained from the USGS California Water Science Center. (b) Distribution of earthquake activities (Magnitude $\geq$ M3) near the experiment scene between 7th and 18th December 2019. All four earthquakes are labeled in the figure. The data is from the USGS Earthquake Hazards Program.(c) Distribution of landslides. The dots are the landslide points. The points with darker color indicate higher confidence of the occurrence of landslides. The data derives from USGS U.S. Landslide Inventory. The experiment scenes are marked as red rectangles in the figures, where A is the flat area and B is the rugged terrain.

the high-accuracy synchronization instruments, and the high-efficiency orbit control strategy should be studied in the future.

APPENDIX A
SUBSIDENCES, EARTHQUAKES, AND LANDSLIDES OF THE EXPERIMENT SCENES

Subsidence, earthquake, and landslides are three main sources generating surface deformations. The distribution of subsidence in the area is shown in Fig. 16 (a). From the subsiding information provided by the USGS California Water Science Center, most of the subsidence in the region is from the excessive groundwater pumping. Other possible reasons that bring deformation are oil extraction and peat loss. Our flat area scene of the TanDEM-X BiDi SAR data suffers the subsidence from groundwater pumping and the rugged terrain scene is likely free of subsidence. The earthquake activities (Magnitude $\geq$ M3) near the experiment scenes between 7th and 18th December 2019 are shown in Fig. 16 (b) and their information is listed in Tab. IV. The data derives from the USGS Earthquake Hazards Program. The magnitudes of all the nearby occurred earthquakes between 7th and 18th December 2019 are less than M4 and the nearest earthquake (Magnitude $\geq$ M3) is point 4, about 40 km away from the rugged terrain scene with a magnitude of M 3.5. Therefore, the deformations of two scenes from the earthquakes during our experiments can be ignored. Fig. 16 (c) provides the distribution of landslide points in the area, where the data is from USGS U.S. Landslide Inventory. According to the figure, the landslide probabilities of two scenes are relatively low.

ACKNOWLEDGMENT

TABLE IV
EARTHQUAKE ACTIVITIES (MAGNITUDE ¿ M3) NEAR THE EXPERIMENT SCENE BETWEEN 7TH AND 18TH DECEMBER 2019. THE DATA IS FROM THE USGS EARTHQUAKE HAZARDS PROGRAM.

No.	Time (UTC)	Position	Intensity	Depth (km)
1	2019-12-17 06:57:45	35.715°N 117.572°W	M 3.6	7.1
2	2019-12-12 11:13:40	35.675°N 117.523°W	M 3.5	9.6
3	2019-12-16 22:15:58	35.671°N 117.527°W	M 3.6	9.3
4	2019-12-16 14:06:50	35.616°N 117.471°W	M 3.5	6.8

REFERENCES

[1] R. Bamler and P. Hartl, "Synthetic aperture radar interferometry," *Inverse problems*, vol. 14, no. 4, p. R1, 1998.

[2] A. Moreira, P. Prats-Iraola, M. Younis, G. Krieger, I. Hajnsek, and K. P. Papathanassiou, "A tutorial on synthetic aperture radar," *IEEE Geoscience and remote sensing magazine*, vol. 1, no. 1, pp. 6–43, Mar. 2013.

[3] R. F. Hanssen, *Radar interferometry: data interpretation and error analysis*. Dordrecht, The Netherlands: Springer, 2001.

[4] S. A.-M. Younes, "Modeling investigation of wet tropospheric delay error and precipitable water vapor content in Egypt," *The Egyptian Journal of Remote Sensing and Space Science*, vol. 19, no. 2, pp. 333–342, Dec. 2016.

[5] C. Hu, Y. Li, X. Dong, R. Wang, C. Cui, and B. Zhang, "Three-dimensional deformation retrieval in geosynchronous sar by multiple-aperture interferometry processing: Theory and performance analysis," *IEEE Transactions on Geoscience and Remote Sensing*, vol. 55, no. 11, pp. 6150–6169, Nov., 2017.

[6] J.-H. Liu, J. Hu, Z.-W. Li, J.-J. Zhu, Q. Sun, and J. Gan, "A method for measuring 3-d surface deformations with insar based on strain model and variance component estimation," *IEEE Transactions on Geoscience and Remote Sensing*, vol. 56, no. 1, pp. 239–250, 2018.

[7] G. Gomba, A. Parizzi, F. De Zan, M. Eineder, and R. Bamler, "Toward operational compensation of ionospheric effects in SAR interferograms: The split-spectrum method," *IEEE Transactions on Geoscience and Remote Sensing*, vol. 54, no. 3, pp. 1446–1461, 2015.

[8] D. Bekaert, R. Walters, T. Wright, A. Hooper, and D. Parker, "Statistical comparison of insar tropospheric correction techniques," *Remote Sensing of Environment*, vol. 170, pp. 40–47, Dec. 2015.

[9] A. Minghelli-Roman and C. Dupouy, "Correction of the water column attenuation: Application to the seabed mapping of the lagoon of New Caledonia using MERIS images," *IEEE Journal of Selected Topics in Applied Earth Observations and Remote Sensing*, vol. 7, no. 6, pp. 2619–2629, June 2014.

[10] N. Adam, "Methodology of a troposphere effect mitigation processor for SAR interferometry," *IEEE Journal of Selected Topics in Applied Earth*

Observations and Remote Sensing, vol. 12, no. 12, pp. 5334–5344, Dec. 2019.

[11] A. Ferretti, A. Fumagalli, F. Novali, C. Prati, F. Rocca, and A. Rucci, "A new algorithm for processing interferometric data-stacks: Squeesar," *IEEE Transactions on geoscience and remote sensing*, vol. 49, no. 9, pp. 3460–3470, Sept. 2011.

[12] A. Hooper, H. Zebker, P. Segall, and B. Kampes, "A new method for measuring deformation on volcanoes and other natural terrains using insar persistent scatterers," *Geophysical Research Letters*, vol. 31, no. 23, 2004. [Online]. Available: https://agupubs.onlinelibrary.wiley.com/doi/abs/10.1029/2004GL021737

[13] D. HO TONG MINH, R. Hanssen, and F. Rocca, "Radar interferometry: 20 years of development in time series techniques and future perspectives," *Remote Sensing*, vol. 12, no. 9, 2020. [Online]. Available: https://www.mdpi.com/2072-4292/12/9/1364

[14] R. Scheiber and A. Moreira, "Coregistration of interferometric sar images using spectral diversity," *IEEE Transactions on Geoscience and Remote Sensing*, vol. 38, no. 5, pp. 2179–2191, 2000.

[15] N. B. Bechor and H. A. Zebker, "Measuring two-dimensional movements using a single insar pair," *Geophysical research letters*, vol. 33, no. 16, 2006.

[16] S. Gudmundsson, F. Sigmundsson, and J. M. Carstensen, "Three-dimensional surface motion maps estimated from combined interferometric synthetic aperture radar and gps data," *Journal of Geophysical Research: Solid Earth*, vol. 107, no. B10, pp. ETG–13, 2002.

[17] F. Guglielmino, G. Nunnari, G. Puglisi, and A. Spata, "Simultaneous and integrated strain tensor estimation from geodetic and satellite deformation measurements to obtain three-dimensional displacement maps," *IEEE Transactions on Geoscience and Remote Sensing*, vol. 49, no. 6, pp. 1815–1826, 2011.

[18] Y. Li, C. Hu, X. Dong, B. Zhang, S. Li, and D. Ao, "Influence of orbit and system parameters on geosynchronous sar multiple-aperture interferometry processing: Analysis and validation," *IEEE Journal of Selected Topics in Applied Earth Observations and Remote Sensing*, vol. 12, no. 6, pp. 1798–1811, 2019.

[19] K. Scipal and M. Davidson, "The saocom-cs mission: Esa's first bistatic and tomographic l-band mission," in *2017 IEEE International Geoscience and Remote Sensing Symposium (IGARSS)*, 2017, pp. 123–124.

[20] P. López-Dekker, H. Rott, P. Prats-Iraola, B. Chapron, K. Scipal, and E. D. Witte, "Harmony: an Earth Explorer 10 Mission Candidate to Observe Land, Ice, and Ocean Surface Dynamics," in *IGARSS 2019 - 2019 IEEE International Geoscience and Remote Sensing Symposium*, 28 July-2 Aug. 2019, Yokohama, Japan, pp. 8381–8384.

[21] C. Chen, "Mitigation of tropospheric insar phase artifacts through differential multisquint processing," in *IGARSS 2004. 2004 IEEE International Geoscience and Remote Sensing Symposium*, vol. 1, 2004, pp. 485–488.

[22] P. López-Dekker, J. Biggs, B. Chapron, A. Hooper, A. Kääb, S. Masina, J. Mouginot, B. B. Nardelli, C. Pasquero, P. Prats-Iraola, P. Rampal, J. Stroeve, and B. Rommen, "The harmony mission: End of phase-0 science overview," in *2021 IEEE International Geoscience and Remote Sensing Symposium IGARSS*, 2021, pp. 7752–7755.

[23] S. Hensley, C. Chen, T. Michel, C. Jones, B. Chapman, and R. Muellerschoen, "Overview and applications of uavsar's multi-squint polarimetric imaging mode," in *POLinSAR 2011*, 24–28 January 2011, Frascati, Italy, pp. 1–8.

[24] M. Kleinherenbrink, A. Korosov, T. Newman, A. Theodosiou, A. S. Komarov, Y. Li, G. Mulder, P. Rampal, J. Stroeve, and P. Lopez-Dekker, "Estimating instantaneous sea-ice dynamics from space using the bistatic radar measurements of earth explorer 10 candidate harmony," *The Cryosphere*, vol. 15, no. 7, pp. 3101–3118, 2021. [Online]. Available: https://tc.copernicus.org/articles/15/3101/2021/

[25] P. Prats-Iraola, P. Lopez-Dekker, F. De Zan, N. Yagüe-Martínez, M. Zonno, and M. Rodriguez-Cassola, "Performance of 3-D surface deformation estimation for simultaneous squinted SAR acquisitions," *IEEE Transactions on Geoscience and Remote Sensing*, vol. 56, no. 4, pp. 2147–2158, Apr. 2017.

[26] Y. Li, P. Lopez-Dekker, L. Iannini, and P. Prats-Iraola, "Performance of 2-d deformation measurements by the multi-static harmony (stereoid) mission," in *IGARSS 2019 - 2019 IEEE International Geoscience and Remote Sensing Symposium*, 2019, pp. 8826–8829.

[27] Y. Li, P. L. Dekker, G. Mulder, L. Iannini, and P. Prats-Iraola, "Differential tropospheric delay estimation by simultaneous multi-angle repeat-pass insar," *IEEE Transactions on Geoscience and Remote Sensing*, 2021.

[28] P. Prats and J. Mallorqui, "Estimation of azimuth phase undulations with multisquint processing in airborne interferometric sar images," *IEEE*

Transactions on Geoscience and Remote Sensing, vol. 41, no. 6, pp. 1530–1533, 2003.

[29] J. Mittermayer, S. Wollstadt, P. Prats-Iraola, P. López-Dekker, G. Krieger, and A. Moreira, "Bidirectional sar imaging mode," *IEEE Transactions on Geoscience and Remote Sensing*, vol. 51, no. 1, pp. 601–614, 2012.

[30] A. Ferretti, A. V. Monti-Guarnieri, C. M. Prati, F. Rocca, D. Massonnet *et al.*, *INSAR Principles A*. ESA publications, 2007.

[31] S. M. Kay, *Fundamentals of Statistical Signal Processing: Estimation Theory*. Prentice Hall, 1997.

[32] N. Wiener, *Extrapolation, Interpolation, and Smoothing of Stationary Time Series*. The MIT Press, 1964.

[33] S. V. Vaseghi, *Advanced digital signal processing and noise reduction*. John Wiley & Sons, 2008.

[34] C. Hu, Y. Deng, W. Tian, and Z. Zhao, "A compensation method for a time–space variant atmospheric phase applied to time-series gb-sar images," *Remote Sensing*, vol. 11, no. 20, p. 2350, 2019.

[35] K. MOGI, "Relations between the eruptions of various volcanoes and the deformations of the ground surfaces around them," *Bull. Earthq. Res. Inst.*, vol. 36, pp. 99–134, 1958.

[36] C. S. Carrano, K. M. Groves, and R. G. Caton, "Simulating the impacts of ionospheric scintillation on L band SAR image formation," *Radio Science*, vol. 47, no. 04, pp. 1–14, Aug. 2012.

[37] G. Krieger, A. Moreira, H. Fiedler, I. Hajnsek, M. Werner, M. Younis, and M. Zink, "Tandem-x: A satellite formation for high-resolution sar interferometry," *IEEE Transactions on Geoscience and Remote Sensing*, vol. 45, no. 11, pp. 3317–3341, 2007.

[38] P. Prats, M. Rodriguez-Cassola, L. Marotti, M. Naninni, S. Wollstadt, D. Schulze, N. Tous-Ramon, M. Younis, G. Krieger, and A. Reigber, "TAXI: A versatile processing chain for experimental TanDEM-X product evaluation," in *2010 IEEE International Geoscience and Remote Sensing Symposium*. IEEE, 2010, pp. 4059–4062.

[39] G. W. Bawden, W. Thatcher, R. S. Stein, K. W. Hudnut, and G. Peltzer, "Tectonic contraction across los angeles after removal of groundwater pumping effects," *Nature*, vol. 412, no. 6849, pp. 812–815, 2001.

[40] S. Liu, *Satellite Radar Interferometry: Estimation of Atmospheric Delay*, 2012. [Online]. Available: https://books.google.co.kr/books?id=y6JxrgEACAAJ

[41] A. Ermakov, R. Park, and B. Bills, "Power laws of topography and gravity spectra of the solar system bodies," *Journal of Geophysical Research: Planets*, vol. 123, no. 8, pp. 2038–2064, 2018.